Applied Catalysis B: Environmental 327 (2023) 122453

Contents lists available at ScienceDirect

Applied Catalysis B: Environmental

journal homepage: www.elsevier.com/locate/apcatb

Single Rh_1Co catalyst enabling reversible hydrogenation and dehydrogenation of N-ethylcarbazole for hydrogen storage

Wenjie Xue [a,1], Hongxia Liu [b,1], Binbin Zhao [c,1], Lixia Ge [a,e], Shuai Yang [d], Minghuang Qiu [a], Jiong Li [d], Wei Han [f], Xinqing Chen [a,e,*]

[a] CAS key Laboratory of Low-carbon Conversion Science and Engineering, Shanghai Advanced Research Institute, Chinese Academy of Sciences, Shanghai 201210, China
[b] School of Chemistry and Chemical Engineering, Wuhan Textile University, Wuhan 430200, China
[c] Department of Materials Science and Engineering; National University of Singapore, Singapore
[d] Shanghai Synchrotron Radiation Facility, Zhangjiang National Lab, Shanghai Advanced Research Institute, Chinese Academy of Sciences, Shanghai 201210, China
[e] University of Chinese Academy of Sciences, Beijing 100049, China
[f] Division of Environment and Sustainability, The Hong Kong University of Science and Technology, Clear Water Bay, Kowloon, Hong Kong SAR China

ARTICLE INFO

Keywords:
Liquid organic hydrogen carrier
Bimetallic catalyst
Hydrogenation
Dehydrogenation
N-ethylcarbazole

ABSTRACT

N-ethylcarbazole (NEC) has been considered one of the most prospective liquid organic hydrogen carriers (LOHCs) for hydrogen storage. However, designing single catalyst capable of driving both hydrogenation of NEC and dehydrogenation of dodecahydro-NEC (12 H-NEC) is of a big challenge. Herein, we develop an atomic-dispersion of Rh with the Co nanoparticles (NPs) to form a Rh_1Co structure maximizing the Rh utilization, which boosts the reversible (de)hydrogenation of NEC, and enables multiple cycles of reversible hydrogen uptake and release. Significantly, a low temperature of 90 °C is realized for the complete hydrogenation (100%), representing one of the lowest temperatures yet reported for the total hydrogenation of NEC. The remarkable catalytic performance of Rh_1Co catalysts is the result of the optimal electronic structure between atomic-dispersion of Rh and Co NPs confirmed by structural characterizations and density functional theory (DFT) calculations, which allowed fast interfacial electron transfer to intermediates.

1. Introduction

It is believed that hydrogen from renewable resources is the optimum energy carrier for the future since it can mitigate dwindling fossil fuel reserves and the environmental issues associated with burning fossil fuels.[1–3] However, the technical issues associated with hydrogen storage restrict the large-scale applications of hydrogen energy due to the low density and potential safety issues of hydrogen.[4,5] To solve this problem, some hydrogen storage technologies such as compressed hydrogen, liquefied hydrogen, metal hydrides, complex hydrides, chemical hydrides and the liquid organic hydrogen carriers (LOHCs) have emerged.[6] In this respect, LOHCs have attracted much attention due to their unique behavior of efficient storage and transport under ambient conditions.[7–11] In this regard, N-ethylcarbazole (NEC) with high hydrogen capacities is an attractive alternate for large-scale energy storage.[12–16] There has been considerable research devoted to the development of a highly efficient catalyst for hydrogen storage.[17–20].

In fact, the Ru, Rh, Pt, Pd-based noble-metal catalysts can hydrogenate NEC or dehydrate 12 H-NEC with excellent performance but it is often limited by high cost.[21–23] Currently, transition metals have been investigated extensively for hydrogenation or dehydrogenation reaction, but they can not compete with noble-metal catalysts the fact that their low activity and stability.[24] However, transition metals based bimetallic catalysts which can enhance catalytic activity through optimization of electronic properties have attracted more attentions. For example, transition metals based bimetallic catalysts such as Rh-Ni, Ru-Ni catalysts show outstanding catalytic activity of hydrogenation and Pd-Cu, Pd-Ni, Pd-Cr catalysts exhibited high reaction rate and selectivity of dehydrogenation.[25–29] Nevertheless, bifunctional transition metal catalysts capable of driving both hydrogenation and dehydrogenation reaction are rare. Seeking inexpensive bifunctional catalysts which can catalyze reversible (de)hydrogenation is an urgent

* Corresponding author at: CAS key Laboratory of Low-carbon Conversion Science and Engineering, Shanghai Advanced Research Institute, Chinese Academy of Sciences, Shanghai 201210, China.
E-mail address: chenxq@sari.ac.cn (X. Chen).
[1] These authors contributed equally to this work.

https://doi.org/10.1016/j.apcatb.2023.122453
Received 13 October 2022; Received in revised form 10 January 2023; Accepted 8 February 2023
Available online 11 February 2023
0926-3373/© 2023 Elsevier B.V. All rights reserved.

need for further economies in resource utilization. In this regard, Co-based catalysts emerged unique electronic reactivity have been investigated for their applications on the hydrogenation of imines, ketones, aldehydes, olefins, and N-heterocycles and dehydrogenation of alcohols but accompanied by poorer catalytic activity compared with noble metal.[30] Concurrently, Rh-based catalysts have been indicated the superior catalytic activity in the hydrogenation reaction but accompanied by undesirable dehydrogenation performance.[15,23] Inspired by the maximization of noble metal and improving the reversible catalytic activity, introducing Rh single-atom with Co is therefore expected to develop a catalyst with excellent reversible activity in the (de)hydrogenation. Thus, it is possible to improve the performance of reversible (de)hydrogenation reaction over Rh single-atom doping of Co-based catalysts, which could be a feasible method to reduce the amounts of precious metals and enhance the performance of the reversible (de)hydrogenation reactions.

Herein, we developed a single reversible bimetallic catalyst with atomic-dispersion of Rh with the Co nanoparticles supported on the γ-Al_2O_3 (named Rh_1Co/γ-Al_2O_3), which can effectively catalyze the reversible (de)hydrogenation reaction of NEC and allow multiple cycles of reversible hydrogen uptake and release. It is noteworthy that the bimetallic Rh_1Co/γ-Al_2O_3 catalysts show excellent catalytic performances on hydrogenation reaction of NEC even at 90 °C, which effectively lowers its hydrogenation reaction temperature. According to the experimental results, a density functional theory (DFT) analysis of the binding energy between Rh and Co, reaction energy profiles, and adsorption energies of substrate molecules on catalyst surfaces was carried out to uncover the optimal electronic structure between the Rh single-atom and Co NPs and the mechanism of the (de)hydrogenate of NEC. The addition of Co atom makes the d band center of Rh atom move to Fermi level, which enhances the adsorption of the reaction substrate on the catalyst and thus improves the catalytic activity.

2. Experimental section

2.1. Chemical and material

N-Ethylcarbazole (97%, Sigma Aldrich) was used as LOHC for both hydrogenation and dehydrogenation reaction; Rhodium(III) chloride hydrate ($RhCl_3{\cdot}xH_2O$, Rh $\geq$ 39.5%) and cobalt nitrate hexahydrate ($Co(NO_3)_2{\cdot}6\ H_2O$) were purchased from Aladdin; Aluminum oxide support (99%) was also from Aladdin.

2.2. Catalysts preparation

For the synthesis of $RhCo/\gamma$-Al_2O_3, 15 mg Rhodium(III) chloride hydrate (Aladdin, Rh $\geq$ 39.5%) was mixed with 150 mg cobalt nitrate hexahydrate (Aladdin, 99%) in 20 ml deionized water at 500 rpm for 20 min. In the next step, 1 g γ-Al_2O_3 (Aladdin, 99%) added into the mixture. After stirring for 12 h, the water was removed at 80 ℃ under stirring. For the RhCo catalyst (named Rh_1Co/γ-Al_2O_3), the loading of Rh was 0.6 wt.% and the loading of Co was 3 wt.%, the mass ratio of Rh to Co is 1:5 and the mole ratio of Rh to Co is 1:8.6. The same preparation of single metal catalyst with same loading, which just removes the second metal from the bimetallic catalyst. The as-prepared catalyst was reduced at 500 ℃ with a heating rate of 2 ℃ per minute under 10% H_2/N_2 mixed gas for 3 h.

2.3. Catalysts characterization

Shimadzu GC-2010 Pro was used to analyze the extracted solution. An X-ray diffractometer (Rigaku, Ultima IV) was used to measure X-ray diffraction spectra. N_2 adsorption-desorption measurements were used to determine the specific surface area and pore size distribution. A probe-corrected TEM JEM-ARM200F was used to collect atomic-resolution high-angle annular dark-field-scanning transmission electron microscopy (HAADF-STEM) images and EDS elemental mapping results. A Nicolet iS50 spectrometer was used to measure CO chemisorption using diffuse reflectance infrared Fourier transform spectroscopy (DRIFTS). Rh L3-edge X-ray absorption near-edge structure (XANES) measurements were conducted on the BL14W1 beamline's X-ray Absorption Fine-Structure (XAFS) station of Shanghai Synchrotron Radiation Facility.

2.4. Catalytic tests

The maximum hydrogen uptake or hydrogen release for the NEC/12 H-NEC system is 5.8 wt% calculated based on the substrate. All H_2-uptake and H_2-release values were calculated by GC and GC-MS taking all the intermediate products into account and based 5.8 wt.% as 100%. For reversible hydrogen storage, the maximum hydrogen uptake is 5.8 wt.%, whereas the maximum hydrogen release is up to the hydrogen uptake in the run.

General procedure for hydrogenation of NEC to 12 H-NEC. NEC (5 g 24.8 mmol) mixed with 0.5 g catalyst were added into a 100 ml stainless steel autoclave. The autoclave was flushed with hydrogen three times and a hydrogen pressure of 60 bar was adjusted. The reactor was heated to corresponding temperature for 1 h under magnetic stirring at 300 rpm.

General procedure for Dehydrogenation of 12 H-NEC to NEC. The 12 H-NEC was obtained by hydrogenation of NEC over the Rh_1CO/γ-Al_2O_3 catalyst. 12 H-NEC (5 g 24.8 mmol) mixed with 0.5 g catalyst were added into a 100 ml stainless steel autoclave. The autoclave was evacuated and flushed with argon for three times. The reactor was heated to corresponding temperature for under magnetic stirring at 300 rpm. Besides, the hydrogen gas was collected quantified and analysed for purity by GC.

2.5. Computational methods

All calculations were performed according to the density functional theory (DFT) approach using the Dmol^3 program package in Materials Studio.[31,32] The generalized gradient approximation (GGA) with the exchange-correlation functional PBE proposed by Perdew-Burke-Ernzerhof was employed to describe the exchange and correlation term.[33,34] In this work, 2.0×10^{-5} Ha, 4.0×10^{-3} Ha•Å^{-1} and 5.0×10^{-3} Å were set for the energy convergence, maximum force and maximum distance. To expand the valence electron function, the double numerical basis set with a polarization *d*-function (DNP) was selected. A $4 \times 4 \times 1$ *k*-point sampling in the surface Brillouin zone was used for Co(111) and $Rh_1Co(111)$ surfaces. The orbital cutoff range was set as medium quality, and 0.005 Hartree is set for the smearing value. An effective core potential (ECP) is used for Co and Rh atoms and all-electron basis sets for other atom.

2.6. Computational models

As for the Co catalyst, the Co(111) surface has the most exposed crystal facets. Thus, the flat FCC-Co(111) surface was employed to investigate the hydrogenation of NEC to 12 H-NEC, a three-layer $p(3 \times 3)$ Co(111) with the optimized lattice parameter of 3.52 Å was applied, which was agreed with the experimental lattice parameter of 3.54 Å, as shown in Fig. S1.

The Rh catalyst with the optimized lattice parameter of 3.76 Å agreed with that of the experimental lattice parameter of 3.80 Å. Therefore, the Rh(111) surface was cleaved from the unit cell with the lattice parameter of 3.76 Å. A $p(2 \times 2)$ surface model with three-layers of Rh atoms was employed, as shown in Fig. S1.

To probe the synergistic effect of between Co and Rh atoms as the sites on the Rh_1Co catalyst controlling the hydrogenation ability, the Co atoms of unit cell were replaced by Rh atoms to construct Rh_1Co bimetallic unit cell, a three-layer $p(3 \times 3)$ $Rh_1Co(111)$ was cleaved to

model the bimetallic Rh_1Co (Fig. S1).

3. Results and discussion

3.1. Electronic structure

The first-principles calculations were conducted to investigate the electronic structure of Co(111), Rh(111) and Rh_1Co(111) surfaces (Fig. S1) based on density functional theory (DFT). The charge distributions of Co(111) results reveal that every Co atom on the pure Co(111) surface was with a small amount of negative charge (−0.01 e) (Fig. 1a). Similarly, Rh atoms on the pure Rh(111) surface had a small amount of negative charge of − 0.012 e (Fig. 1b). On the Rh_1Co(111) catalyst, for the first layer of Rh_1Co(111), Rh and Co atoms are both with negative charge (−0.027, −0.014 and −0.013 e) (Fig. 1c). However, for the second layer of Rh_1Co(111), Rh and Co atoms are both with positive charge (0.093, 0.016, 0.015, 0.014 and 0.013 e) (Fig. 1d), indicating that charge transfer is directed from subsurface layer to surface layer with Rh and Co atoms serving as electronic donors to accomplish bimetallic synergetic effects and electroactivity was primarily found on Rh surface sites. Meanwhile, charge density difference calculations were used to study the interactions and electronic structure of Rh and Co atoms (Fig. 1e-g). Charge density is depleted around Co atoms, while it accumulates around Rh atoms. The electron transfer effect is evident when Co atoms release electrons to the Rh atoms, in line with the above charge distributions analysis.

Moreover, spin-polarized partial density of states (PDOS) were applied to analyze electron density transfer from Co to Rh shown in Fig. 1h-m. The *d*-band center values of Co(111), Rh(111) and Rh_1Co(111) surfaces were − 1.41, − 2.23 and − 1.77 eV, confirming that Rh plays a crucial role in electron transfer. At the surface Rh of Rh_1Co(111), the d-band center of Rh was slightly lower and the valence state of Co was conserved, maintaining a proper H-bonding strength without overbonding. In contrast, both bulk Rh and bulk Co shifted their d-band centers deeper (further away from the Fermi level), becoming more electron-rich in the process. Bulk electrons could be transferred efficiently in this electronic environment, suggesting that the introduction of Rh to Co catalysts was with more anti-bonding states being occupied.

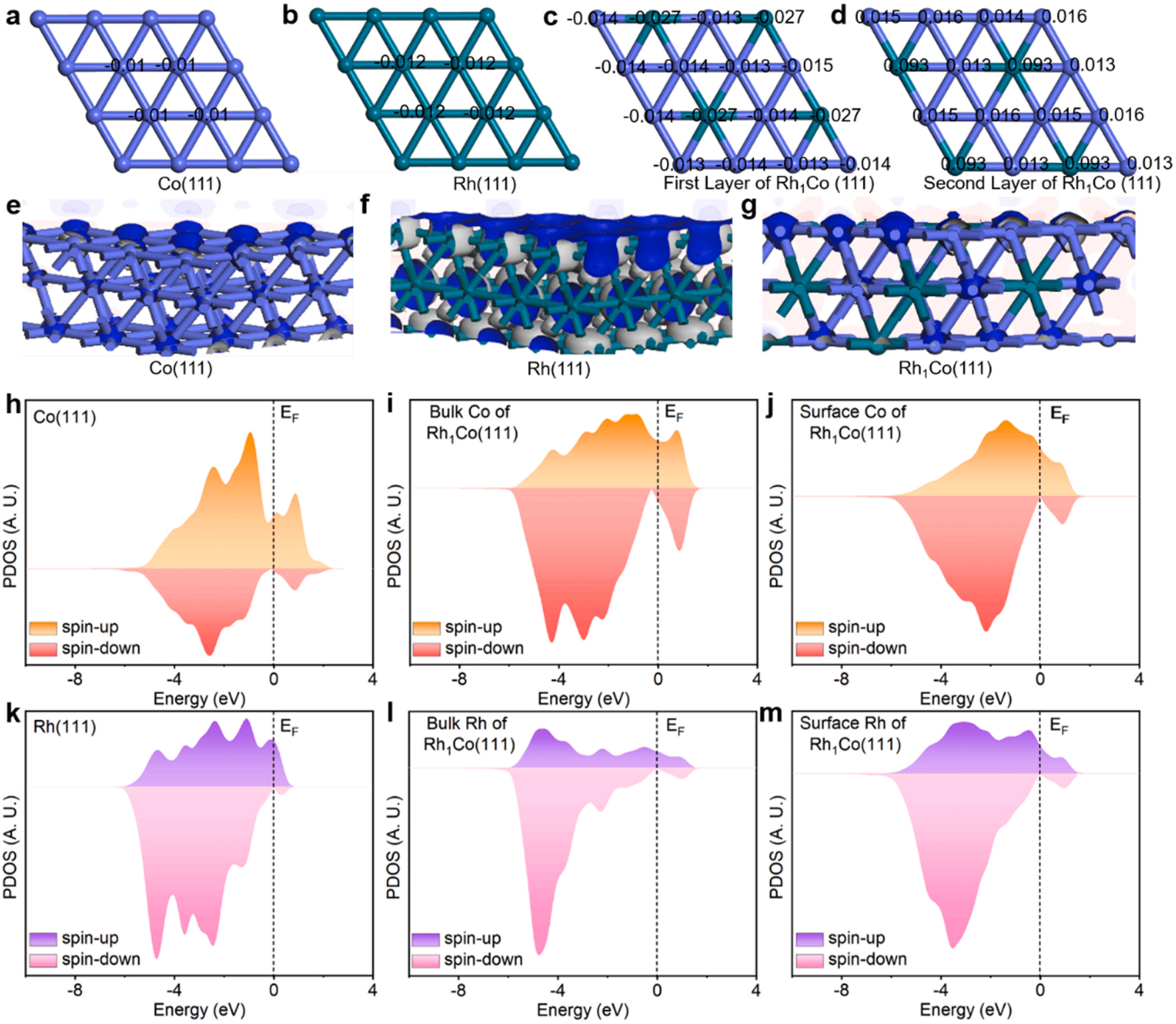

Fig. 1. Electronic structure of different catalysts. (a-d) The mulliken charge distribution of Co(111), Rh(111) and Rh_1Co(111), (e-g) The differential charge distribution of Co(111), Rh(111) and Rh_1Co(111), blue represents electron depletion and red represents electron enrichment, respectively and (h-m) PDOS for the surface atoms of Co(111), Rh(111) and Rh_1Co(111). The light blue and green balls represent the Co and Rh atoms.

The addition of Co atom increases the valence state of Rh, and makes the d band center of Rh atom move to Fermi level, which will improve the reaction energy and promote the reaction kinetics.

3.2. Catalyst synthesis and characterization

A series of monometallic or bimetallic catalysts with γ-Al_2O_3 supports (Fig. S2) were precisely fabricated using a method of wet chemistry. Based on N_2 sorption-desorption isotherms (Fig. S3), the specific surface area of Rh_1Co/γ-Al_2O_3 is 157.9 $m^2 \cdot g^{-1}$ (Brunauer-Emmett-Teller model) which is larger than unsupported γ-Al_2O_3 (127.0 $m^2 \cdot g^{-1}$) and the bi-modal pore size distribution of Rh_1Co/γ-Al_2O_3 is decreased slightly from 19.9 nm to 17.2 nm after the deposition of the metals. The powder X-ray diffraction (XRD) patterns of the different catalysts were shown in Fig. 2a and the traces of crystalline Rh, Co and Rh_1Co NPs cannot be found due to the small loading. Rh single-atom catalysts are easily synthesized and used in other reactions at small loadings.[35–37] Based on STEM image, the Rh_1Co NPs were homogenously distributed on the γ-Al_2O_3 (1.10 nm) (Fig. 2b). The HADDF-STEM image for the Rh_1Co/γ-Al_2O_3 catalyst displays isolated bright dots in Fig. 2c due to the dispersed Rh single atoms on Rh_1Co/γ-Al_2O_3 highlighted with white circles. Then, ex-situ Fourier-transform extended X-ray absorption fine structure (EXAFS) was carried out to study the coordination situation around Rh atoms in Rh_1Co/γ-Al_2O_3. The fourier transform (FT) EXAFS curves of the Rh_1Co/γ-Al_2O_3, Rh_2O_3 and Rh foil were depicted in Fig. 3d. It was obvious that Rh_1Co/γ-Al_2O_3 showed one prominent coordination peak at 1.63 Å different from that in Rh_2O_3 of 1.53 Å and in Rh foil of 2.37 Å, which could be ascribed to Rh-O-Co bond in Rh_1Co/γ-Al_2O_3 since the Co metals are easily oxidized under ex-situ conditions.[38,39] This result further proves that Co atoms are surrounded by Rh single atoms. However, the observation of Rh-O-Co bonds in EXAFS after oxidation of the particles cannot evidence that the all Rh atoms are surrounded by Co atoms only, as there is massive restructuring associated with the oxidation process, and it need further study. In order to further understand the surface structure of Rh_1Co catalyst, DRIFTS CO chemisorption measurements were carried out as showed in Fig. 2e, in light of the fact that CO was sensitive probe of Rh ensembles.[40–42] The monometallic catalysts of Rh/γ-Al_2O_3 presented three species: bridged CO focus on 1858 cm^{-1}, linear Rh^0-CO bond focus on 2056 cm^{-1}, and $Rh(CO)_2$ focus on 2093 cm^{-1} and 2031 cm^{-1}. The red-shift of $Rh(CO)_2$ focus on 2093 cm^{-1} and 2031 cm^{-1} were clearly observed on Rh_1Co/γ-Al_2O_3. This phenomenon provided strong evidence for the electronic interaction between Co and Rh with the strengthened electron density of Rh. Notably, the bridged CO and linear Rh^0-CO bond were disappeared only left with $Rh(CO)_2$ on Rh_1Co/γ-Al_2O_3 compared with those on Rh/γ-Al_2O_3 again implying that the Rh atom were isolated by the surrounding Co atoms in majority forming the bimetallic NPs, which was in good accordance with HADDF-STEM micrograph and FT EXAFS curves (Fig. 2c-d). Moreover, X-ray photoemission spectroscopy (XPS) measurements in the Rh 3d region uncovered the electronic interaction between Rh and Co (Fig. 2f). For Rh_1Co/γ-Al_2O_3 sample, we observed a significant positive binding energy shift of Rh 3d by 0.6 eV with respect to that of Rh/γ-Al_2O_3, which is due to the charge transfer between Rh and Co.[43] The experimental results suggested that charge transfer may have occurred and the surface electronic structure was tended to the pure Rh, which is in agreement with the calculated charge density difference (Fig. 1e-g). The in-situ Co 2p XPS spectra for both the two catalysts show main peaks at the binding energy of 777.58 and 792.78 eV assignable to Co $2p_{3/2}$ and Co $2p_{1/2}$ of Co^0, respectively (Fig. S4), suggesting the valence of Co is main metallic

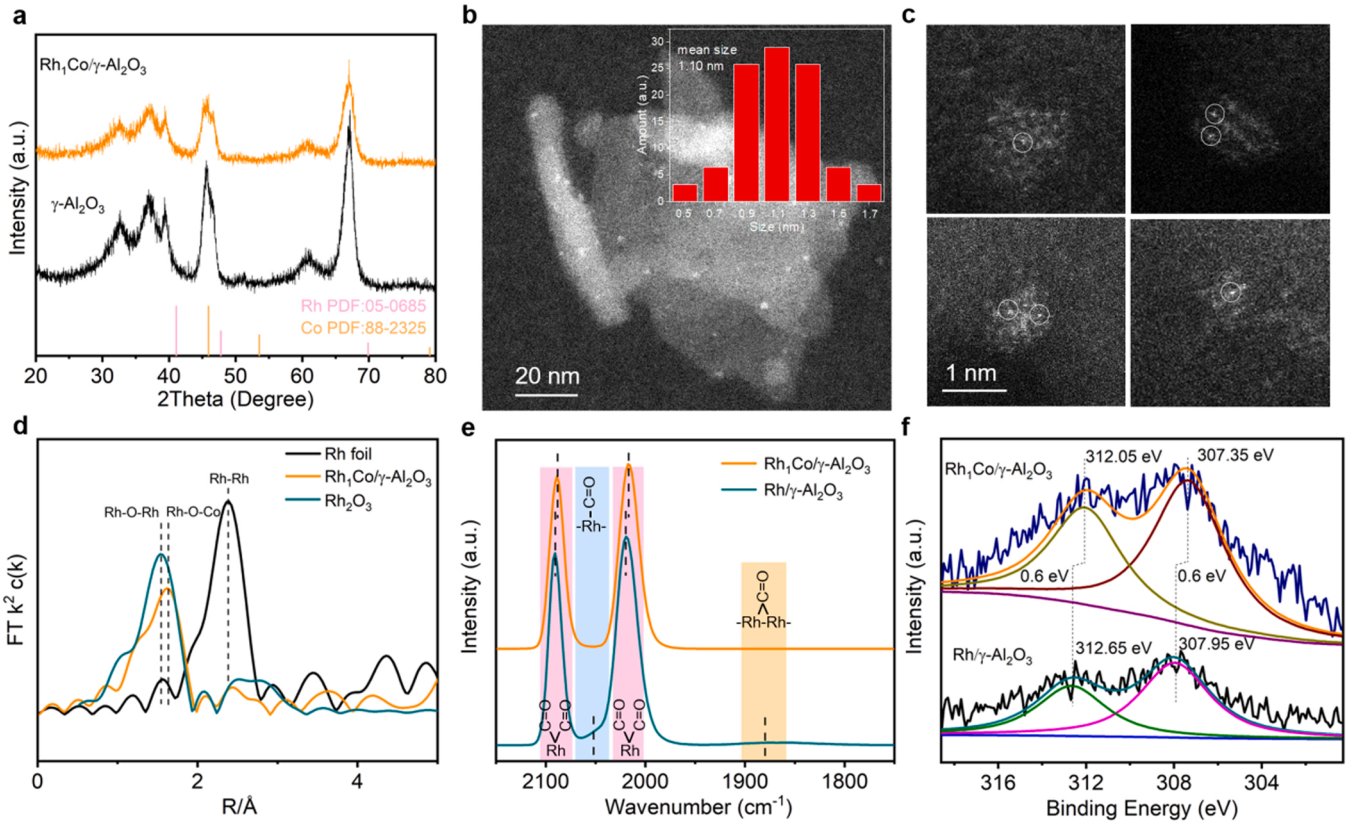

Fig. 2. Characterization. (a) XRD patterns of the Rh_1Co/γ-Al_2O_3 and γ-Al_2O_3 samples. (b) HAADF-STEM image of Rh_1Co/γ-Al_2O_3, and the size distribution, (c) Several representative HAADF-STEM image of Rh_1Co/γ-Al_2O_3, (d) Fourier transform of Rh K-edge EXAFS of Rh_1Co/γ-Al_2O_3, Rh_2O_3 and Rh foil reference in the real space at the Rh K-edge. (e) *In-situ* DRIFTS CO chemisorption of the Rh_1Co/γ-Al_2O_3 and Rh/γ-Al_2O_3 samples at the CO saturation coverage. (f) XPS spectra of Rh_1Co/γ-Al_2O_3 and Rh/γ-Al_2O_3 samples in the Rh 3d region.

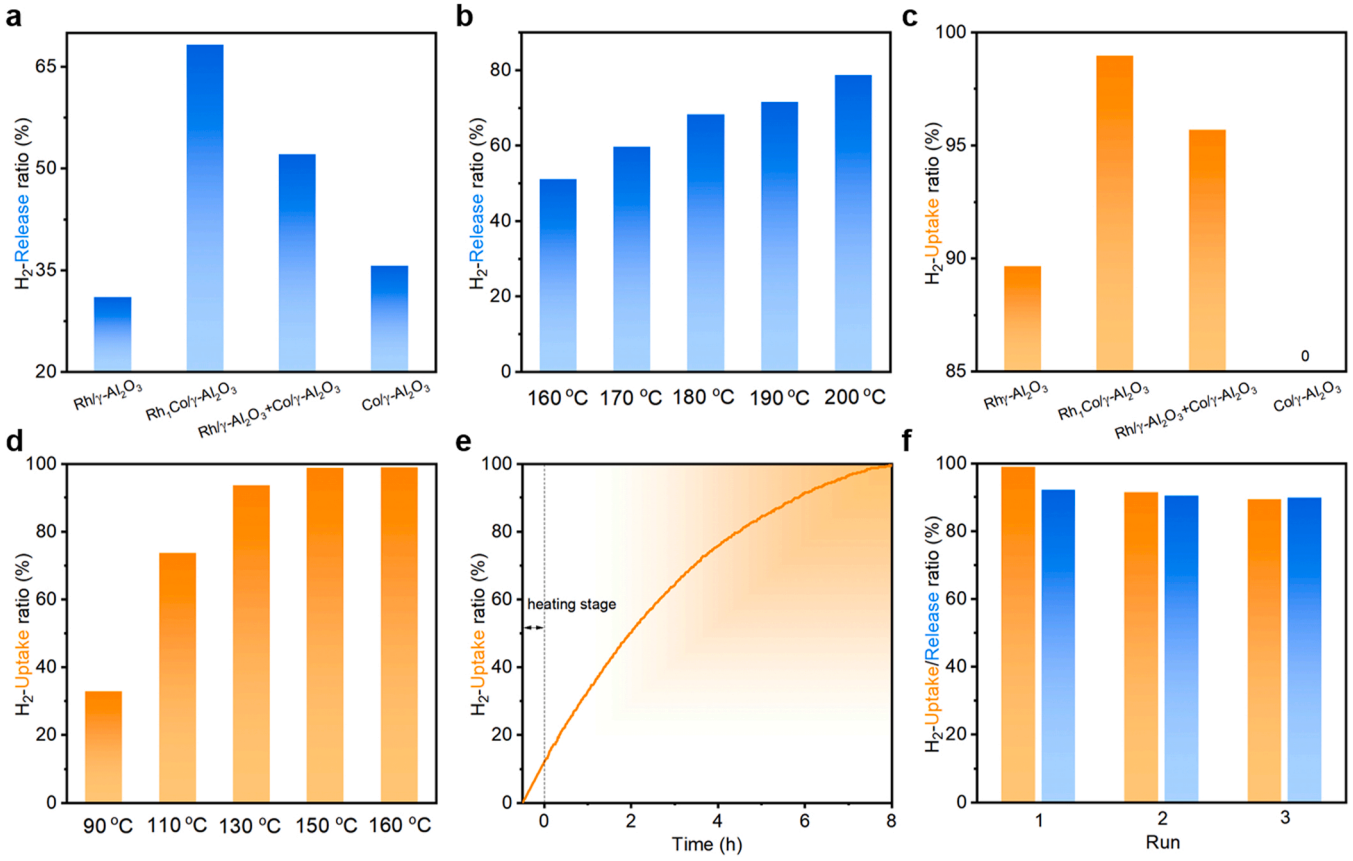

Fig. 3. Catalytic performance comparison for (de)hydrogenation. (a) Dehydrogenation of 12 H-NEC on different catalysts. 180 °C, 2 h, 5.0 g reactant, 0.5 g catalyst. (b) Dehydrogenation of 12 H-NEC on $Rh_1Co/\gamma\text{-}Al_2O_3$ catalysts at different temperatures. 5.0 g reactant, 0.5 g catalyst, 2 h. (c) Hydrogenation of NEC on different catalysts. 160 °C, 5 g reactant, $P(H_2) = 60$ bar, 0.5 g catalyst, 1 h. (d) Hydrogenation of NEC on $Rh_1Co/\gamma\text{-}Al_2O_3$ catalysts at different temperatures. $P(H_2) = 60$ bar, 5 g reactants, 0.5 g catalyst, 1 h. (e) Hydrogenation of NEC on $Rh_1Co/\gamma\text{-}Al_2O_3$ catalysts at 90 °C. $P(H_2) = 60$ bar, 5 g reactant, 0.5 g catalyst. (f) Catalyst reusability test: 0.5 g catalyst, 5.0 g N-ethylcarbazole,; hydrogenation: $P(H_2) = 60$ bar, 5 g reactant, 0.5 g catalyst, 1 h; dehydrogenation: 200 °C, 5.0 g reactant, 0.5 g catalyst, 6 h.

state. And we also observed a slight negative binding energy shift of Co 2p by 0.1 eV for $Rh_1Co/\gamma\text{-}Al_2O_3$ with respect to that of $Co/\gamma\text{-}Al_2O_3$ due to the charge transfer between Rh and Co (Fig. S4).

3.3. Catalytic performance

The bimetallic Co and Rh species with a strong electronic interaction may render the unique $Rh_1Co/\gamma\text{-}Al_2O_3$ catalyst a multifunctional catalyst that is suitable for the reversible (de)hydrogenation reactions. Thus, the reversible (de)hydrogenation reactions were evaluated on the bimetallic $Rh_1Co/\gamma\text{-}Al_2O_3$ catalyst, monometallic $Rh/\gamma\text{-}Al_2O_3$ and $Co/\gamma\text{-}Al_2O_3$ catalysts which were conducted in a batch reactor (Fig. S5) and gas chromatography (GC) and GC-mass spectrometry (MS) measurements were used to calculate hydrogen uptake and release (Fig. S6). The dehydrogenation reaction was firstly evaluated at common-used temperatures of 180 °C within 2 h (Fig. 3a). And the $Rh_1Co/\gamma\text{-}Al_2O_3$ catalysts show excellent performance on dehydrogenation with hydrogen release ratio of 68.28% for 12 H-NEC than the monometallic $Rh/\gamma\text{-}Al_2O_3$ catalysts (31.03%) and monometallic $Co/\gamma\text{-}Al_2O_3$ catalysts (35.69%). Similarly, the $Rh_1Co/\gamma\text{-}Al_2O_3$ catalysts also show much better performance on dehydrogenation (68.28%) than physical mixture of $Co/\gamma\text{-}Al_2O_3$ and $Rh/\gamma\text{-}Al_2O_3$ catalysts (52.08%). The monometallic $Rh/\gamma\text{-}Al_2O_3$ catalysts prefer to exhibit excellent performance on hydrogenation of NEC with hydrogen uptake ratios of 89.73% compared to the unfavorable dehydrogenation of 12 H-NEC with hydrogen release ratio of 31.03%. Next, the dehydrogenation reaction was evaluated at different temperature over the $Rh_1Co/\gamma\text{-}Al_2O_3$ catalyst. As shown in Fig. 3b, it is reasonable that higher reaction temperature results in higher hydrogen release ratio. Additionally, H_2 was collected, quantified, and analyzed for purity by GC (Fig. S8). The hydrogenation reaction was then evaluated at common-used temperatures of 160 °C within 1 h (Fig. 3c). Remarkably, the $Rh_1Co/\gamma\text{-}Al_2O_3$ catalysts show most excellent performance with hydrogen uptake ratios of 98.96% for NEC than the monometallic $Rh/\gamma\text{-}Al_2O_3$ catalysts (89.73%) and monometallic $Co/\gamma\text{-}Al_2O_3$ catalysts (0%). In addition, as we know, the temperature plays great influence on the hydrogenation reaction. In order to further compare the catalytic performance, the hydrogenation reaction temperature was lowered to 130 °C (Fig. S7). And it is worth noting that the $Rh_1Co/\gamma\text{-}Al_2O_3$ catalysts also show most excellent performance with hydrogen uptake ratios of 93.6% for NEC than the monometallic $Rh/\gamma\text{-}Al_2O_3$ catalysts (73.8%) and monometallic $Co/\gamma\text{-}Al_2O_3$ catalysts (0%) at 130 °C. The monometallic $Co/\gamma\text{-}Al_2O_3$ catalysts are almost inactive for the hydrogenation of NEC. In order to exclude the contribution of electronic interactions in the $Rh_1Co/\gamma\text{-}Al_2O_3$ catalysts to our observed improvement of hydrogenation, another physical mixture sample of $Co/\gamma\text{-}Al_2O_3$ and $Rh/\gamma\text{-}Al_2O_3$ were also tested for comparison. As shown in Fig. 3c, the corresponding hydrogen uptake ratios for NEC on physical mixture of $Co/\gamma\text{-}Al_2O_3$ and $Rh/\gamma\text{-}Al_2O_3$ catalysts are 95.69%, worse than that of the $Rh_1Co/\gamma\text{-}Al_2O_3$ catalyst. Then, we tried to lower the hydrogenation temperature to investigate the hydrogenation performance of the $Rh_1Co/\gamma\text{-}Al_2O_3$ catalysts (Fig. 3d). Intriguingly, the hydrogen uptake ratio for NEC is still as high as 32.88% within 1 h even when the hydrogenation temperature is decreased to 90 °C and the hydrogen uptake ratios for NEC can reach as high as 100% when the time is extended to

8 h (Fig. 3e), which is, to our best knowledge, the lowest hydrogenation temperature compared to previous reports. The monometallic Co/γ-Al_2O_3 catalysts have superior catalytic dehydrogenation activity than the noble-metal Rh/γ-Al_2O_3 catalysts with hydrogen release ratio of 35.69% but with poor catalytic hydrogenation activity. Significantly, the bimetallic Rh_1Co based catalysts exhibit enhanced catalytic activity not only for the hydrogenation of NEC reactions but also for the dehydrogenation of 12 H-NEC reactions. In addition, the lower catalytic activity and selectivity over a physical mixture of Co/γ-Al_2O_3 and Rh/γ-Al_2O_3 in comparison to that of Rh_1Co/γ-Al_2O_3 undoubtedly exhibit that the improved hydrogenation performance of NEC, which is mainly ascribed to electronic interactions between the Rh single-atom and the Co NPs in the Rh_1Co/γ-Al_2O_3 catalysts. Supplementary Table S1–2 provides a detailed breakdown of the product distribution. Moreover, the reusability of the Rh_1Co/γ-Al_2O_3 catalysts was studied and there was barely any loss of hydrogen storage capacity after repeating this procedure three times (Fig. 3f).

Based on the results, we developed a schematic diagram showing that the Rh_1Co/γ-Al_2O_3 catalysts boosts (de)hydrogenation of NEC along with the plausible reaction paths as presented in Fig. 4.

3.4. DFT calculation

The DFT along with periodic slab models Co(111), Rh(111) and Rh_1Co(111) were used to uncover the reaction pathway (Fig. 5-6). [44–46] Honestly, as compared to the energetic profiles, the adsorption of substrate molecules are associated strongly with hydrogenation activity. Fig. 5 presented the adsorption energy of H, NEC and nH-NEC (n = 4, 6, 8 and 12) on Co(111), Rh(111) and Rh_1Co(111) surfaces. From Fig. 5a, it can be found that the adsorption energy of H on Co(111), Rh(111) and Rh_1Co(111) are − 292. 8, − 268.7 and − 288.7 kJ mol^{-1}, indicating the strong interaction between H and Co, which slows down the overall dehydrogenation of 12 H-NEC. Thus, the introduction of Rh into Co can balance the interaction between metal and H atom and also accelerates the (de)hydrogenation reaction. Moreover, the adsorption energy of NEC on Co(111), Rh(111) and Rh_1Co(111) are − 113.6, 181.9 and − 102.8 kJ·mol^{-1}. The corresponding adsorption energy of 4 H-NEC on Co(111), Rh(111) and Rh_1Co(111) were − 99.5, − 147.2, − 89.3 kJ·mol^{-1}, For 6 H-NEC, the adsorption energy on Co(111), Rh (111) and Rh_1Co(111) were − 99.0, − 132.3 and − 112.0 kJ·mol^{-1}. For the adsorption of 8 H-NEC on Co(111), Rh(111) and Rh_1Co(111), the corresponding adsorption energy were − 40.3, − 63.1 and − 44.6 kJ·mol^{-1}. For 12 H-NEC, the adsorption energy on Co(111), Rh (111) and Rh_1Co(111) were − 65.9, 79.9 and 64.2 kJ·mol^{-1}. Pure Rh catalyst showed stronger interaction with reaction substrate and intermediate (NEC, 4 H-NEC, 6 H-NEC, 8 H-NEC and 12 H-NEC), indicating that Rh catalyst is favour of the hydrogenation of NEC[47,48]. However, pure Co catalysts slow down the interaction with reaction substrate and intermediate. It is worth noting that bimetallic Rh_1Co/γ-Al_2O_3 catalyst not only balance the interaction between metal and H atom, but also balance the interaction between metal and reaction substrate and intermediate, resulting in better catalytic performance for hydrogenation of NEC. In addition, we also build another 4 * 4 supercell of Co(111) and calculated the adsorption energy of 12-NEC(Fig. S9). Compared with 3 * 3 Co(111), the adsorption energy on 4 * 4 Co(111) for 12 H-NEC is − 68.2 kJ·mol^{-1}, which indicates that there is little difference with 3 * 3 Co(111) of − 65.9 kJ·mol^{-1}, indicating that 3 * 3 Co(111) can be applied.

Then, the reaction energy (ΔH/kJ·mol^{-1}) of hydrogenation reaction from NEC to 12 H-NEC on the Rh(111) and Rh_1Co(111) surfaces (Fig. S10-11) along with the energy profile (Fig. 6) were performed to evaluate the mechanism. For the Rh(111) catalysts, the hydrogenation processes on this result were all exothermic with reaction energies of − 139.0, − 52.5, − 76.8 and − 11.8 kJ·mol^{-1}, which was account for that the Rh(111) was in favor of hydrogenation, instead, the dehydrogenation is difficult since the reversibility of the two processes, especially the dehydrogenation reaction of 8 H-NEC to 12 H-NEC with reaction energies of 139.0 kJ·mol^{-1}. On the contrary, the hydrogenation from 8 H-NEC to 12 H-NEC on the Rh_1Co(111) were exothermic by − 52.5 kJ·mol^{-1}, which proved that the NEC is easy to fully hydrogenate to 12 H-NEC as revealed by our experiments (Fig. 3). In addition, overall moderate hydrogenation reaction energy on Rh_1Co(111) confirm that the reversible catalytic performance for the (de)hydrogenation on Rh_1Co(111) catalysts is largely due to the synergistic effect between Rh and Co atoms. Based on the above analysis, the DFT calculations are in line with our experimental results.

4. Conclusion

In summary, a single reversible Rh_1Co/γ-Al_2O_3 bimetallic catalysts with atomic-dispersion of Rh applied to reversible (de)hydrogenate of NEC were successfully developed for the hydrogen storage. The obtained Rh_1Co/γ-Al_2O_3 catalysts exhibited an excellently reversible activity and allow several cycles of reversible hydrogen uptake and release. Significantly, a low temperature of 90 °C is enough for the hydrogenation with a high hydrogen uptake ratio of 100%. The favorable processes for the (de)hydrogenation on Rh_1Co/γ-Al_2O_3 were attributed to the optimal electronic structure between Rh single-atom and Co NPs. DFT analysis of binding energy between Rh and Co, reaction energy profiles, and adsorption energies of substrate molecules on catalytic surface were

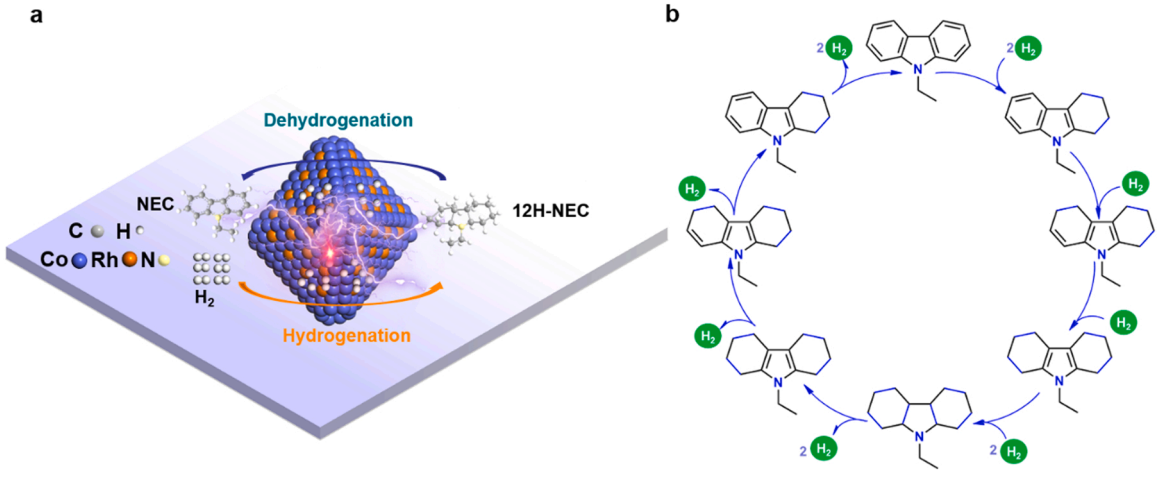

Fig. 4. (a) A schematic diagram illustrating the (de)hydrogenation of NEC on the bimetallic Rh_1Co/γ-Al_2O_3. (b) the plausible reaction paths of (de)hydrogenation of NEC.

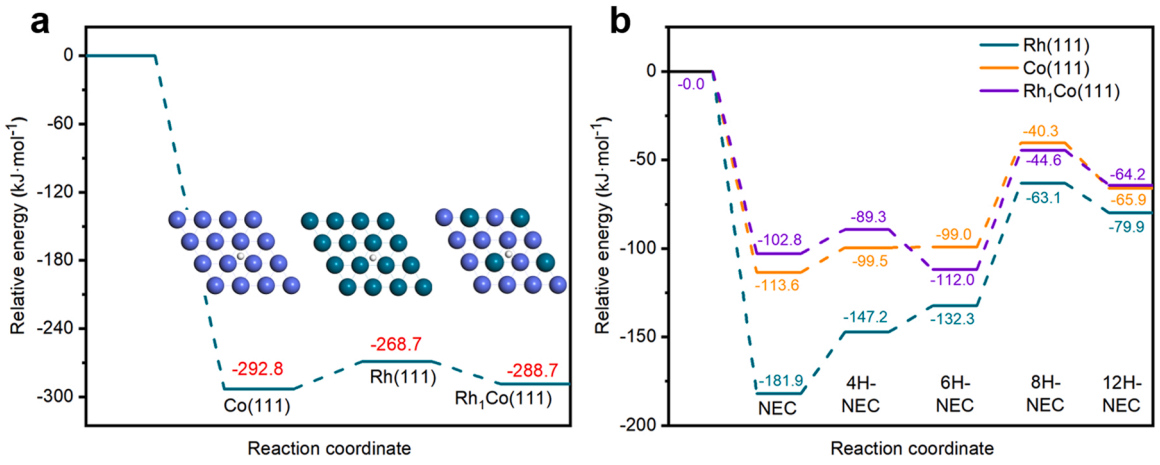

Fig. 5. (a) Adsorption energy for H on the Co(111), Rh(111) and $Rh_1Co(111)$ facets. (b) Adsorption energy for related intermediates on the Co(111), Rh(111) and $Rh_1Co(111)$ facets.

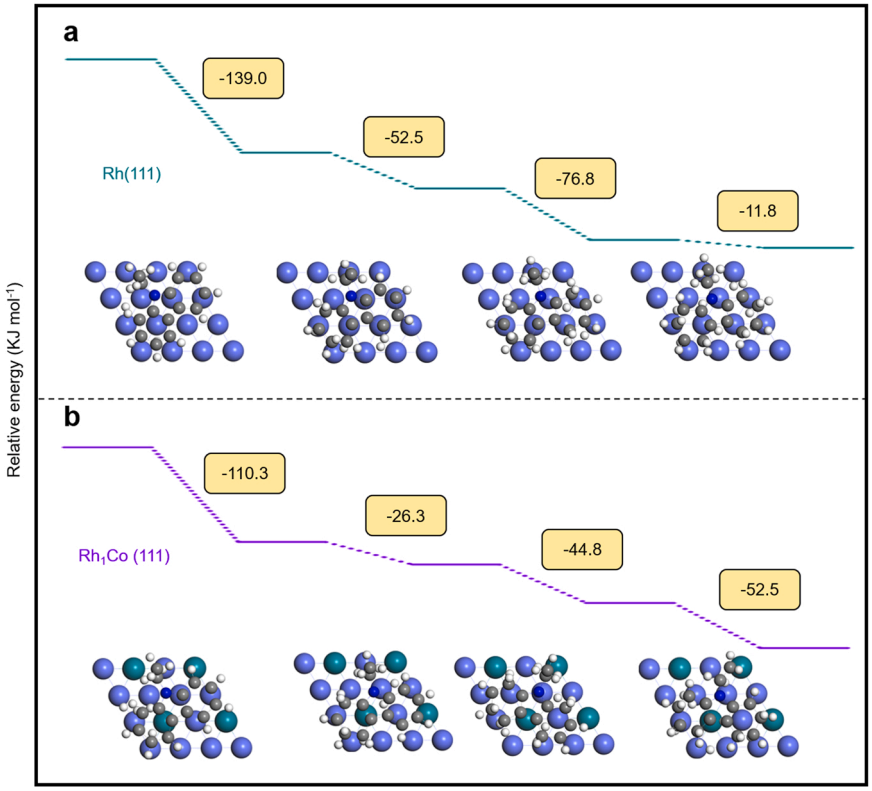

Fig. 6. (a, b) The hydrogenation of NEC to 12 H-NEC on the Rh(111) and $Rh_1Co(111)$ facets. The light blue, green, blue, white and gray balls represent the Co, Rh, N, H, and C atoms, respectively.

carried out to uncover the optimal electronic structure between the Rh single-atom and Co NPs and the plausible mechanism of the (de)hydrogenate of NEC. The addition of Co atom increased the valence state of Rh, and made the d band center of Rh atom move to Fermi level, which improves the reaction energy and promotes the reaction kinetics. In addition, bimetals significantly enhanced the adsorption and hydrogen spillover effects of the reaction substrate on the catalyst, which further promoted the improvement of the catalytic activity.

CRediT authorship contribution statement

Wenjie Xue: Experimental, Characterization, Writing – original draft. **Hongxia Liu:** DFT calculation. **Binbin Zhao:** Experimental, Characterization. **Lixia Ge**: Formal analysis, Methodology. **Shuai Yang**: EXAFS analysis. **Minghuang Qiu**: Formal analysis, Methodology. **Jiong Li**: EXAFS analysis. **Wei Han**: Investigation, Characterization. **Xinqing Chen**: Supervision, Methodology, Funding acquisition, Writing – review & editing.

Declaration of Competing Interest

The authors declare that they have no known competing financial interests or personal relationships that could have appeared to influence the work reported in this paper.

Data Availability

Data will be made available on request.

Acknowledgements

The authors acknowledge financial supports from National Key Research and Development Program of China (2022YFE0208300) and Natural Science Foundation of China (22078354, 21776295).

Appendix A. Supporting information

Supplementary data associated with this article can be found in the online version at doi:10.1016/j.apcatb.2023.122453.

References

[1] G. Sievi, D. Geburtig, T. Skeledzic, A. Bösmann, P. Preuster, O. Brummel, P. Wasserscheid, Towards an efficient liquid organic hydrogen carrier fuel cell concept, Energy Environ. Sci. 12 (2019) 2305–2314.
[2] L. Schlapbach, A. Züttel, Hydrogen-storage materials for mobile applications, Nature 414 (2001) 353–358.
[3] C. Dong, Z. Gao, Y. Li, M. Peng, M. Wang, Y. Xu, D. Ma, Fully exposed palladium cluster catalysts enable hydrogen production from nitrogen heterocycles, Nat. Catal. 5 (2022) 485–493.
[4] Q.L. Zhu, Q. Xu, Liquid organic and inorganic chemical hydrides for high-capacity hydrogen storage, Energy Environ. Sci. 8 (2015) 478–512.
[5] T. He, P. Pachfule, H. Wu, Q. Xu, P. Chen, Hydrogen carriers, Nat. Rev. Mater. 1 (2016) 16067.
[6] M. Niermann, S. Drünert, M. Kaltschmitt, K. Bonhoff, Liquid organic hydrogen carriers (LOHCs)–techno-economic analysis of LOHCs in a defined process chain, Energy Environ. Sci. 12 (2019) 290–307.
[7] D. Mellmann, P. Sponholz, H. Junge, M. Beller, Formic acid as a hydrogen storage material-development of homogeneous catalysts for selective hydrogen release, Chem. Soc. Rev. 45 (2016) 3954–3988.
[8] Y.Q. Zou, N. von Wolff, A. Anaby, D. Milstein, Ethylene glycol as an efficient and reversible liquid-organic hydrogen carrier, Nat. Catal. 2 (2019) 415–422.
[9] A. Boddien, D. Mellmann, F. Gärtner, R. Jackstell, H. Junge, P.J. Dyson, M. Beller, Ethylene glycol as an efficient and reversible liquid-organic hydrogen carrier, Science 333 (2011) 1733–1736.
[10] J.F. Hull, Y. Himeda, W.H. Wang, B. Hashiguchi, R. Periana, D.J. Szalda, E. Fujita, Reversible hydrogen storage using CO_2 and a proton-switchable iridium catalyst in aqueous media under mild temperatures and pressures, Nat. Chem. 4 (2012) 383–388.
[11] C. Gunanathan, Y. Ben-David, D. Milstein, Direct synthesis of amides from alcohols and amines with liberation of H_2, Science 317 (2007) 790–792.
[12] P. Preuster, C. Papp, P. Wasserscheid, Liquid organic hydrogen carriers (LOHCs): toward a hydrogen-free hydrogen economy, Acc. Chem. Res. 50 (2017) 74–85.
[13] S. Zhang, Z. Xia, M. Zhang, Y. Zou, H. Shen, J. Li, X. Chen, Y. Qu, Boosting selective hydrogenation through hydrogen spillover on supported-metal catalysts at room temperature, Appl. Catal. B: Environ. 297 (2021), 120418.
[14] R. Yamaguchi, C. Ikeda, Y. Takahashi, Homogeneous catalytic system for reversible dehydrogenation-hydrogenation reactions of nitrogen heterocycles with reversible interconversion of catalytic species, J. Am. Chem. Soc. 131 (2009) 8410–8412.
[15] K.M. Eblagon, K. Tam, S.C.E. Tsang, Comparison of catalytic performance of supported ruthenium and rhodium for hydrogenation of 9-ethylcarbazole for hydrogen storage applications, Energy Environ. Sci. 5 (2012) 8621–8630.
[16] H. Chen, H. Shuang, W. Lin, X. Li, Z. Zhang, J. Li, J. Fu, Tuning interfacial electronic properties of palladium oxide on vacancy-abundant carbon nitride for low-temperature dehydrogenation, ACS Catal. 11 (2021) 6193–6199.
[17] Y. Wu, H. Yu, X. Li, A rare earth hydride supported ruthenium catalyst for the hydrogenation of N-heterocycles: boosting the activity via a new hydrogen transfer path and controlling the stereoselectivity, Chem. Sci. 10 (2019) 10459–10465.
[18] K.M. Eblagon, S.C.E. Tsang, Structure-reactivity relationship in catalytic hydrogenation of heterocyclic compounds over ruthenium black-Part A: Effect of substitution of pyrrole ring and side chain in N-heterocycles, Appl. Catal. B: Environ. 160 (2014) 22–34.
[19] D. Forberg, T. Schwob, R. Kempe, Single-catalyst high-weight% hydrogen storage in an N-heterocycle synthesized from lignin hydrogenolysis products and ammonia, Nat. Commun. 7 (2016) 13201.
[20] T. Zhu, M. Yang, X. Chen, Y. Dong, Z. Zhang, H.S. Cheng, A highly active bifunctional Ru–Pd catalyst for hydrogenation and dehydrogenation of liquid organic hydrogen carriers, J. Catal. 378 (2019) 382–391.
[21] Y. Dong, M. Yang, P. Int. J. Mei, Dehydrogenation kinetics study of perhydro-N-ethylcarbazole over a supported Pd catalyst for hydrogen storage application, Hydrog. Energy 41 (2016) 8498–8505.
[22] L. Ge, M. Qiu, Y. Zhu, S. Yang, W. Li, W. Li, Z. Jiang, X. Chen, Synergistic catalysis of Ru single-atoms and zeolite boosts high-efficiency hydrogen storage, Appl. Catal. B: Environ. 319 (2022), 121958.
[23] W. Xue, H. Liu, B. Mao, H. Liu, M. Qiu, C. Yang, X. Chen, Y. Sun, Reversible hydrogenation and dehydrogenation of N-ethylcarbazole over bimetallic Pd-Rh catalyst for hydrogen storage, Chem. Eng. J. 421 (2020), 127781.
[24] K.M. Eblagon, K. Tam, K.M.K. Yu, S.C.E. Tsang, Comparative study of catalytic hydrogenation of 9-ethylcarbazole for hydrogen storage over noble metal surfaces, J. Phys. Chem. C. 116 (2012) 7421–7429.
[25] M. Arnende, C. Gleichweit, K. Werner, S. Schernich, W. Zhao, M.P.A. Lorenz, O. Hofert, C. Papp, M. Koch, P. Wasserscheid, M. Laurin, H.P. Steinruck, J. Libuda, Model catalytic studies of liquid organic hydrogen carriers: dehydrogenation and decomposition mechanisms of dodecahydro-N-ethylcarbazole on Pt(111), ACS Catal. 4 (2014) 657–665.
[26] H. Liu, C. Zhou, W. Li, W. Li, M. Qiu, X. Chen, Y. Sun, Ultralow Rh bimetallic catalysts with high catalytic activity for the hydrogenation of N-Ethylcarbazole, ACS Sustain. Chem. Eng. 9 (2021) 5260–5267.
[27] C. Li, M. Yang, Z. Liu, Z. Zhang, T. Zhu, X. Chen, H. Cheng, Ru–Ni/Al_2O_3 bimetallic catalysts with high catalytic activity for N-propylcarbazole hydrogenation, Catal. Sci. Tech. 10 (2020) 2268–2276.
[28] B. Wang, T. Chang, T. Fang, Component controlled synthesis of bimetallic PdCu nanoparticles supported on reduced graphene oxide for dehydrogenation of dodecahydro-N-ethylcarbazole, Appl. Catal. B: Environ. 251 (2019) 261–272.
[29] L.M. Kustov, A.L. Tarasov, O.A. Kirichenko, Microwave-activated dehydrogenation of perhydro-N-ethylcarbazol over bimetallic Pd-M/TiO_2 catalysts as the second stage of hydrogen storage in liquid substrates, Int. J. Hydrog. Energy 42 (2017) 26723–26729.
[30] Y. Yang, D. Rao, Y. Chen, S. Dong, B. Wang, X. Zhang, M. Wei, Selective hydrogenation of cinnamaldehyde over Co-based intermetallic compounds derived from layered double hydroxides, ACS Catal. 8 (2018) 11749–11760.
[31] J.K. Nørskov, T. Bligaard, J. Rossmeisl, C.H. Christensen, Towards the computational design of solid catalysts, Nat. Chem. 1 (2009) 37–46.
[32] B. Delley, From molecules to solids with the DMol3 approach, J. Chem. Phys. 113 (2000) 7756–7764.
[33] A. Mehranfar, M. Izadyar, Theoretical evaluation of N-alkylcarbazoles potential in hydrogen release, Int. J. Hydrog. Energy 42 (2017) 9966–9977.
[34] D. Tian, H. Zhang, J. Zhao, Structure and structural evolution of Agn (n= 3-22) clusters using a genetic algorithm and density functional theory method, Solid State Commun. 144 (2007) 174–179.
[35] L. Wang, W. Zhang, S. Wang, Z. Gao, Z. Luo, X. Wang, J. Zeng, Atomic-level insights in optimizing reaction paths for hydroformylation reaction over Rh/CoO single-atom catalyst, Nat. Commun. 7 (2016) 14036.
[36] P. Shen, X. Li, Y. Luo, N. Zhang, X. Zhao, K. Chu, Ultra-efficient N_2 electroreduction achieved over a rhodium single-atom catalyst (Rh_1/MnO_2) in water-in-salt electrolyte, Appl. Catal. B: Environ. 316 (2022), 121651.
[37] P. Gao, G. Liang, T. Ru, X. Liu, H. Qi, A. Wang, F.E. Chen, Phosphorus coordinated Rh single-atom sites on nanodiamond as highly regioselective catalyst for hydroformylation of olefins, Nat. Commun. 12 (2021) 4698.
[38] J.O. Ehresmann, P.W. Kletnieks, A. Liang, V.A. Bhirud, O.P. Bagatchenko, E.J. Lee, J.F. Haw, Evidence from NMR and EXAFS studies of a dynamically uniform mononuclear single-site zeolite-supported rhodium catalyst, Angew. Chem. Int. Ed. 118 (2006) 588–590.
[39] J. Guo, C. Xie, K. Lee, N. Guo, J.T. Miller, M.J. Janik, C. Song, Improving the carbon resistance of Ni-based steam reforming catalyst by alloying with Rh: a computational study coupled with reforming experiments and EXAFS characterization, ACS Catal. 1 (2011) 574–582.
[40] J.C. Matsubu, V.N. Yang, P. Christopher, Isolated metal active site concentration and stability control catalytic CO_2 reduction selectivity, J. Am. Chem. Soc. 137 (2015) 3076–3084.
[41] J.T. Yates, T.M. Duncan, S.D. Worley, Infrared spectra of chemisorbed CO on Rh, J. Chem. Phys. 70 (1979) 1219.
[42] X. Chen, M. Qiu, S. Li, C. Yang, L. Shi, S. Zhou, G. Yu, L. Ge, X. Yu, Z. Liu, N. Sun, K. Zhang, H. Wang, M. Wang, L. Zhong, Y. Sun, Gamma-Rays Irradiation Accelerates Crystallization of Mesoporous Zeolites, Angew. Chem. Int. Ed. 59 (2020) 11325–11329.
[43] X. Zheng, Y. Lin, H. Pan, L. Wu, W. Zhang, L. Cao, T. Yao, Grain boundaries modulating active sites in RhCo porous nanospheres for efficient CO_2 hydrogenation, Nano Res 11 (2018) 2357–2365.
[44] M.A. Petersen, J.A. van den Berg, I.M. Ciobica, P. van Helden, Revisiting CO activation on Co catalysts: impact of step and kink sites from DFT, ACS Catal. 7 (2017) 1984–1992.
[45] M. Birgersson, C.O. Almbladh, M. Borg, J.N. Andersen, Density-functional theory applied to Rh(111) and CO/Rh(111) systems: Geometries, energies, and chemical shifts, Phys. Rev. B 67 (2003), 045402.
[46] L. Ding, N. Ishida, M. Murakami, K. Morokuma, sp^3–sp^2 vs sp^3–sp^3 C–C Site selectivity in rh-catalyzed ring opening of benzocyclobutenol: a DFT study, J. Am. Chem. Soc. 136 (2014) 169–178.
[47] T.W. Kim, M. Kim, S.K. Kim, Y.N. Choi, M. Jung, H. Oh, Y.-W. Suh, Remarkably fast low-temperature hydrogen storage into aromatic benzyltoluenes over MgO-supported Ru nanoparticles with homolytic and heterolytic H_2 adsorption, Appl. Catal. B: Environ. 286 (2021), 119889.
[48] B. Wang, Y. Chen, T. Chang, Z. Jiang, Z. Huang, S. Wang, C. Chang, S. Yang, T. Fang, Facet-dependent catalytic activities of Pd/rGO: exploring dehydrogenation mechanism of dodecahydro-N-ethylcarbazole, Appl. Catal. B: Environ. 266 (2020), 118658.